Bright short-wavelength infrared organic light-emitting devices

Yuan Xie
Institute of Polymer Optoelectronic Materials and Devices, State Key Laboratory of Luminescent Materials and Devices, South China University of Technology

Wansheng Liu
Institute of Polymer Optoelectronic Materials and Devices, State Key Laboratory of Luminescent Materials and Devices, South China University of Technology https://orcid.org/0000-0003-1355-7345

Wanyuan Deng
South China University of Technology

Haimei Wu
Xi'an Key Laboratory of Liquid Crystal and Organic Photovoltaic Materials, State Key Laboratory of

Weiping Wang
Xi'an Key Laboratory of Liquid Crystal and Organic Photovoltaic Materials, State Key Laboratory of

Yichuan Si
Institute of Polymer Optoelectronic Materials and Devices, State Key Laboratory of Luminescent Materials and Devices, South China University of Technology

Xiaowei Zhan
Peking University https://orcid.org/0000-0002-1006-3342

Chao Gao
Xi'an Key Laboratory of Liquid Crystal and Organic Photovoltaic Materials, State Key Laboratory of Fluorine & Nitrogen Chemicals, Xi'an Modern Chemistry Research Institute https://orcid.org/0000-0002-2559-8964

Xian-Kai Chen
City University of Hong Kong https://orcid.org/0000-0002-8580-7246

Hongbin Wu (hbwu@scut.edu.cn)
Institute of Polymer Optoelectronic Materials and Devices, State Key Laboratory of Luminescent Materials and Devices, South China University of Technology https://orcid.org/0000-0003-2770-6188

Junbiao Peng
South China University of Technology

Yong Cao
South China University of Technology/Institute of Polymer Optoelectronic Materials and Devices,State Key Laboratory of Optoelectronic Materials and Devices/State Key Laboratory of Luminescent Materi

Article

Keywords:

Posted Date: March 16th, 2022

DOI: https://doi.org/10.21203/rs.3.rs-1147211/v1

Version of Record: A version of this preprint was published at Nature Photonics on September 29th, 2022. See the published version at https://doi.org/10.1038/s41566-022-01069-w.

Bright short-wavelength infrared organic light-emitting devices

Yuan Xie[1,5*], Wansheng Liu[1,5], Wanyuan Deng[1,5], Haimei Wu[2,5], Weiping Wang[2], Yichuan Si[1], Xiaowei Zhan[3], Chao Gao[2*], Xian-Kai Chen[4*], Hongbin Wu[1*], Junbiao Peng[1] & Yong Cao[1]

[1]Institute of Polymer Optoelectronic Materials and Devices, State Key Laboratory of Luminescent Materials and Devices, South China University of Technology, Guangzhou 510640, P. R. China

[2]Xi'an Key Laboratory of Liquid Crystal and Organic Photovoltaic Materials, State Key Laboratory of Fluorine & Nitrogen Chemicals, Xi'an Modern Chemistry Research Institute, Xi'an, Shaanxi 710065, P. R. China

[3]Department of Materials Science and Engineering, College of Engineering, Key Laboratory of Polymer Chemistry and Physics of Ministry of Education, Peking University, Beijing 100871, P. R China

[4]Department of Chemistry, Department of Materials Science and Engineering, City University of Hong Kong, Kowloon 999077, Hong Kong SAR, P.R. China

[5]These authors contributed equally: Yuan Xie, Wansheng Liu, Wanyuan Deng, Haimei Wu.

*Correspondence to: xieyuan@scut.edu.cn (Y. X.), chaogao1974@hotmail.com (C. G.), xche22@cityu.edu.hk (X. C.), hbwu@scut.edu.cn (H. W.)

Abstract

Organic light-emitting devices (OLEDs) emissive in short-wavelength infrared (SWIR) region are attractive for ground-breaking applications in biosensors, biomedical imaging and next-generation optoelectronic devices. However, fabrication of such devices with high radiance has not yet been achieved, owing to an intrinsic limitation imposed by the energy-gap law, which leads to extremely low emission efficiency. Here we report that acceptor-donor-acceptor (A-D-A) type molecules with high co-planarity, rigidity of π-conjugated backbones, extremely small reorganization energy and electron-phonon coupling factor are capable of simultaneously providing strongly suppressed non-radiative recombination rate, and high operation stability at high current density. We achieve electrically driven SWIR with irradiance of 3.9 mW cm^{-2} (corresponding to 7% of direct sunlight infrared irradiance), which is the brightest emission to date and surpasses that of any previously reported SWIR OLEDs sixty-fold. These findings should open a wide avenue to a new class of organic SWIR light sources for broad applications.

Organic semiconductors with advantageous electronic and optoelectronic properties have enabled demonstration of high-performance organic light-emitting devices (OLEDs) with emission covering the visible, near-ultraviolet and near-infrared parts of the electromagnetic spectrum[1-5]. There has been long-standing demand for the development of electrically driven short-wavelength infrared (SWIR, 1000–2000 nm) [6,7] light sources in view of their broad range of applications, including optical communications[3-5], night-vision surveillance[3,4,6] and remote sensing[8]. Recent emerging applications in biological imaging[9-11], medical analyses[12] and infrared spectroscopy[9] for health, food and environmental monitoring require the development of bright, biocompatible SWIR emitters, as longer imaging wavelengths promise lower light scattering, deeper tissue penetration depth and superior spatiotemporal resolution[9-11] compared to the visible and near infrared (NIR, 700–1000 nm) counterparts. More recently, SWIR light sources are integrated in smart phone for providing security authentication and photonic sensing functionalities[4,13], thereby enabling fast and convenient face and iris recognition. Currently, high-performance SWIR emitters are generally found in group III-V compound semiconductors[7,14]. However, the manufacturing of SWIR LEDs with these inorganic semiconductors usually involves complicated epitaxial growth on crystalline substrates, thus increasing their cost and restricting their potential for integration of optoelectronic devices.

Among the emerging candidates for large area planar SWIR light sources, organic light-emitting devices are particularly unique as they have shown to combine advantages of high-throughput fabrication at extremely low costs, light weight, mechanical flexibility, tunable chemical, physical properties and emission wavelength,

and compatibility with large area[1-3]. Furthermore, purely organic fluorescent emitters are heavy-metal-free, which is potentially more biocompatible and environmentally sustainable, thus ideal for health, food and environmental applications where biocompatibility, toxicity and environmental issues must be considered[4]. To translate these advantages to widespread SWIR applications, high radiance/brightness OLEDs are necessary to obtain satisfactory performance and for device miniaturization. However, unlike the success in the visible[1] and NIR region[3-5,13,15,16], bright OLEDs in the SWIR range have not been demonstrated so far. The main reason for this could be ascribed to the limitation subject to the energy-gap law[3-5], which predicts an exponentially increased non-radiative decay rate with decreasing energy gap in organic solids, as a result of the increased electron-phonon coupling between the excited and ground states. This limitation indicates, if the energy-gap law is strictly valid, long wavelength emission from organic solids is extremely weak and there is a major bottleneck for extending the emission to longer wavelengths.

Despite such major fundamental hurdle, extensive research efforts have been dedicated to narrowing the energy gap and realizing electroluminescence beyond the visible region, *i.e.,* 700-1000 nm near-infrared emission in organic solids by adopting rational strategies used for visible emitters. These strategies generally involve several key considerations[3-5], such as extending conjugation length, reducing bond length alternation (corresponding to greater π-electron delocalization), introduction of appropriate donor–acceptor charge transfer units and use of triplet[17] or doublet excitons[18]. As a result, nowadays organic emitters available for NIR OLEDs includes

mainly organometallic phosphorescent complex[19,20], organic ionic dyes[21], conjugated polymers[22], organic compounds containing donor–acceptor charge transfer chromophores[3,5,18,23-25], thermally activated delayed fluorescent (TADF) materials[26] and doublet emitters[18]. In 2020, Wei *et al.* reported state-of-the-art phosphorescent NIR OLEDs by exploiting a series of 5-(2-pyridyl) pyrimidinate Pt(II) complexes, achieving electroluminescence peaked at 930 nm, with an external quantum efficiency (EQE) of 2.14% and a remarkable maximum radiant exitance of 13.06 mW cm^{-2} (ref. 20). Yu *et al.* demonstrated high-performance fluorescent NIR OLEDs based on anthracene cored emitters, which exhibit electroluminescence peaks at 838 nm and 916 nm with an EQE of 0.58% and 0.07%, while the maximum radiant exitance is 2.8 mW cm^{-2} and 0.29 mW cm^{-2}, respectively[27]. More recently, progress in fluorescent NIR OLEDs was made by Minotto *et al*., who achieved an EQE of 1.1% with EL spectrum peaked at 850 nm and a maximum radiant exitance of 1.9 mW cm^{-2}, respectively[13]. However, previous studies showed that OLEDs that emitting at longer wavelengths (*e.g.*, beyond 1000 nm extending into the SWIR region) always suffer from severe non-radiative recombination loss, leading to either low EQE of the order of 0.01%[22,28] or low maximum radiant exitance of 0.06 mW cm^{-2} (despite a state-of-the-art EQE of 0.28%)[3].

Ever since the recent emergence of a new class of acceptor−donor−acceptor (A-D-A) type aromatic fused-ring electron acceptors, the development of organic solar cells has now entered into a new era featuring the coincidence of efficient charge separation and low voltage losses[29]. Owing to the strong intramolecular charge transfer effect and the rigid planarity configuration of the fused rings, π-electron

delocalization in these A-D-A type organic semiconductors is enhanced, producing reduction in the bandgap and a greater oscillator strength that increases the near-infrared absorption coefficients. Moreover, A-D-A type organic semiconductors show several additional great merits that are essential for minimizing energy loss in organic solar cells. These include a sharp optical absorption edge, suppressed non-radiative recombination rate, low energetic disorder and high luminescence (radiative recombination) yield, which play important role in obtaining high photovoltage[30]. According to the reciprocity relation existing between light absorption and emission[31], such organic semiconductors that is ideal for solar cells is likewise ideal for light-emitting devices.

Results and discussion

Computational results. Prior to an attempt to exploit A-D-A type organic semiconductors for SWIR emitter applications, the density functional theory (DFT) and time-dependent DFT (TD-DFT) approaches at the ωB97XD/6-31G(d,p) level with the optimally tuned ω parameter are employed to study the structural regularity and the excited-state properties for three typical narrow bandgap molecules with low photon energy loss in organic solar cells, i. e., Y11[(ref. 30)], IDSe-4Cl (**Supplementary Methods**) and COTIC-4F[32] (see **Fig. 1a–c** for the chemical structures and **methods** for computational details). Our DFT calculation results displayed a small dihedral angle of 14° for Y11, whilst nearly planar structures with negligible torsion in their relaxed geometries were observed for IDSe-4Cl and COTIC-4F (**Supplementary Fig.1**). The success of this design strategy was confirmed extended emissive exciton wavefunctions, as shown by the calculated natural transition orbitals (NTO)

describing the first singlet (S_1) excited states (see **Fig. 1d)**. The NTO hole and electron wavefunctions of the S_1 excitons spread the whole π-conjugated backbones, implying strong electronic couplings between the donor and acceptor moieties. In conjunction with the alternating electron-withdrawing and electron-releasing moieties that incurs intramolecular charge transfer effect[4,5], the enhanced wave function delocalization and the extended planarity of the A-D-A molecules have ensured minimized optical band gaps[33] of 1.37, 1.27 and 1.17 eV for Y11, IDSe-4Cl and COTIC-4F (**Supplementary Fig. 2**), respectively, which is envisaged to led to SWIR emissions beyond 1000 nm. More importantly, the significant spatial overlaps ($O_{h/e}$) between the NTO-hole and NTO-electron give rise to unprecedentedly large oscillator strengths of 2.3, 3.2 and 3.0 for Y11, IDSe-4Cl and COTIC-4F, respectively[34], corresponding to their high radiative recombination rates, as discussed below.

Photophysical properties and numerical simulations. To further illustrate their potential as a new type of SWIR emitters, the absorption and photoluminescence (PL) spectra of three molecules were measured. As shown in **Fig. 2a–c**, the thin films of three molecules exhibit sharp absorption bands with a dominant peak slightly above the optical gap and a low-energy shoulder adjacent to it. Owing to its overwhelmingly high oscillator strength, transition from ground state (S_0) to the first excited state (S_1) induces intense absorption peak, which, consequently, surpasses the intensities of other transitions. Following Kasha's rule, fast thermalization occurs exclusively before through radiative recombination to the ground state, such that the higher energy electronic transitions should play a minimal part in PL, and the PL spectra are dominated by $S_1 \rightarrow S_0$ transition only. The low energy shoulders found in the PL spectra are thus confirmed to be an outcome of high-frequency vibrational modes of

the molecules[35,36].

Meanwhile, we propose a model based on established theories[37-39] to describe these vibrational pathways through which unfavorable non-radiative recombination takes place. According to the model, the optical emission intensity $I_{emission}$ at specific photon energy hv is proportional to the oscillator strength f embodying the electronic transition dipole moment, and the Franck-Condon-weighted density of states (FCWD) that describes the wave function overlap between the vibrational levels of excited and ground states, while adopting Born-Oppenheimer approximation (**Supplementary Note 1**):

$$\frac{I_{emission}(hv)}{(hv)^3} \propto f \cdot FCWD(hv) \tag{1}$$

with

$$FCWD(hv) = \frac{e^{-s}}{\sqrt{4\pi\lambda_s k_B T}} \sum_{j=0}^{\infty} \frac{S^j}{j!} exp\left[\frac{-(E_g - hv - j\hbar\overline{v}_v - \lambda_s)^2}{4\lambda_s k_B T}\right] \tag{2}$$

in which $FCWD(hv)$ is further governed by three vibrational parameters: low-frequency reorganization energy λ_s that describes the conformational changes of the molecule and its surroundings upon excitation, energy of high-frequency vibrational mode $\hbar\overline{v}_v$ in which $\overline{v}_v$ averages the frequencies of atomic vibrations within the molecule, and electron-phonon coupling factor S related to the high-frequency reorganization energy λ_v that results from atomic displacements upon charging to the aforementioned mean phonon energy $\hbar\overline{v}_v$, by $S = \lambda_v/(\hbar\overline{v}_v)$. The lineshape of the reduced emission spectra where the emission spectra are divided by $(hv)^3$ are therefore intricately modulated by these vibrational parameters through Equation (2).

Careful fitting of the measured PL spectra via Equations (1) and (2) has enabled the extraction of vibrational parameters of our molecules, as shown in **Fig. 2d–f**, with

the details provided in **Supplementary Note 2**. Very low λ_s ranging from 0.045 to 0.06 eV are obtained for these molecules, which correspond to their narrow linewidths. The observations are also consistent with the significantly reduced Stokes shifts, as indicated in **Fig. 2a–c**. Overall, these findings suggest that photo-excitation and the subsequent decays barely trigger the deformation of molecular geometries, which is a result of their enhanced planarity and rigidity in A-D-A molecules. Thanks to their narrow linewidths, mean phonon energy $h\overline{\nu}_v$ ranging from 0.12 to 0.14 eV for the molecules can be readily determined by the small energy shift from the pronounced 0-0 peaks to 0-1 vibrational shoulders (**Supplementary Fig. 3**). As such, the experimental values are considerably lower than the characteristic value of 0.16 eV for the predominant carbon-carbon bonds and ring stretching modes in organic molecules[35,38,40]. Finally, the electron-phonon coupling factors S are extracted to be in the range of 0.7–0.9 for the molecules. The estimated total reorganization energies (λ_{SI}=λ_S + λ_v) including the two parts due to the low-frequency and high-frequency vibrations via the fitting of the emission spectrum lineshapes, i.e., 0.16, 0.14, and 0.15 eV, are very consistent with our TDDFT calculation results, i.e., 0.13, 0.13, and 0.15 eV, implying the reliability of our fitting via Equations (1) and (2).

Substituting all the previously obtained parameters into Fermi's golden rule, the rate constant of non-radiative recombination can be derived:

$$k_{nr} = \frac{2\pi}{h} V^2 FCWD(0) \quad (3)$$

with the electronic coupling V approximated by the generalized Mulliken-Hush (GMH) method[39,41].

The photoluminescence quantum yield (PLQY) can be eventually determined via PLQY $= \frac{k_r}{k_r+k_{nr}}$, where k_r and k_{nr} are the rate constants of radiative and non-radiative recombination, respectively. The calculated PLQYs for a set of

representative parameters are plotted against band gap in **Fig. 2g**. The PLQYs show dramatic decreases when lowering the band gap, following the 'energy-gap law', leading to relatively lower PLQY for narrow band gap molecule. The results of the experimentally determined PLQYs are included for direct comparison. Nevertheless, further numerical simulations show that the reduced λ_s, $h\overline{\nu}_v$ and S of the molecules reported herein significantly suppress the non-radiative recombination rate (**Supplementary Fig. 4**), while enhanced oscillator strength f is beneficial for an increased radiative recombination rate, eventually giving rise to higher PLQYs (calculated value of 0.1-10% for bandgap ranging from 1.1 eV to 1.3 eV) for the molecules.

Under these circumstances, A-D-A molecules with conjugation extension[42] and/or enhanced planarity and rigidity in their π-conjugated backbones[43] that enable reduced reorganization energies are indeed ideal candidates capable of enhancing long wavelength emission and emission efficiency simultaneously. To make further improvement of PLQY, other approach such as heavy atom substitution or halogenations for retarding high-frequency vibration modes could prove an effective molecular design strategy to lower mean phonon energy $h\overline{\nu}_v$ in A-D-A molecules, as discussed below.

In fact, although the k_{nr} for a series of A-D-A type organic semiconductors extracted from the experimentally achieved PLQY (**Supplementary Table 1**) and time-resolved PL decay transients (**Supplementary Fig. 5**) increase with decreasing bandgap, but much less pronounced compared with the prediction of the energy-gap law (**Fig. 3a**). Additionally, the extracted k_r shows a striking increase with increasing oscillator strength (**Fig. 3b**), which is consistent with the model calculations (**Supplementary Fig. 4g**). It turns out that the trend imposed by the

energy-gap law can be counteracted to some extent by appropriate electronic couplings between relevant states and superior photophysical properties, thus yielding more efficient emission, as confirmed by our PLQY measurements (**Fig. 3c**). For example, we determined that the PLQY of Y11 film was about 8.13%, while the PLQY of a wider bandgap (~1.59 eV) molecule i-IEICO-4F is about 5.73% (**Supplementary Table 1 & Supplementary Note 3**). Furthermore, model calculations show reducing $h\overline{v}_v$ by 0.02 eV or lowering S by 0.3 correspond to nearly an order of magnitude enhancement for PLQY, as illustrated in **Supplementary Fig. 4 i–j**.

Device characterization and demonstrations. The analyses above suggest that A-D-A type organic semiconductors have promising potential for realizing high-performance SWIR OLEDs. To validate our findings, we fabricate electroluminescent devices using these narrow bandgap molecules including Y11, IDSe-4Cl and COTIC-4F as emitters, and other representative narrow bandgap A-D-A type molecules (with the chemical structures and the corresponding absorption spectra shown in **Supplementary Fig. 6** and **Supplementary Fig. 7**, respectively) as well. The device architecture employed was ITO/PEDOT: PSS/Emissive layer/PDINO/Ag (ITO, indium tin oxide; PEDOT: PSS, poly(3,4-ethylenedioxythiophene) polystyrene sulfonate; PDINO, (N,N-dimethyl-ammonium N-oxide)propyl perylene diimide). The OLEDs performance characteristics, including current density-radiance-voltage (*J-R-V)*, electroluminescence (EL) spectra and external quantum efficiency (EQE) dependence on current density (EQE-*J*), are shown in **Fig. 4** and **Supplementary Fig. 8**, while key parameters are summarized in **Table 1**. The electroluminescence (EL) spectra of the devices demonstrate tuning with peak ranging from 810 to 1230 nm

(**Fig. 4a**).

It is worth noting that OLEDs based on i-IDSe-4Cl (peaked at 843 nm) and Y11 (peaked at 945 nm) show a maximum EQE of 0.54% and 0.33% (**Table 1**), respectively, which is among the highest efficiencies reported in fluorescent NIR OLEDs[27]. Moreover, the devices exhibit high maximum radiant exitance of 12-14 mW cm^{-2} that is twice those values of the best fluorescent emitter[27] and comparable to state-of-the-art phosphorescent NIR OLEDs with similar EL spectra (**Supplementary Fig. 9**)[20]. More importantly, broad tunability of the A-D-A type organic semiconductors has enabled bright SWIR electroluminescence spanning from 1000 to 1300 nm and beyond, which is extremely rare in organic material systems. Among them, devices based on IDSe-4F and IDSe-4Cl show the best performance (**Table 1**), which have an EQE of 0.13 % an 0.12 % with EL peak at 1080 nm and 1110 nm, respectively. These two molecules are analogs of the reported ultra-narrow bandgap A-D-A type conjugated molecules[44], in which indacenodiselenophene (IDSe) is used as the electron-donating core to achieve red-shifted absorption and large extinction coefficients[45]. Besides, a long-branched alkoxy group was introduced to the inserted thiophene unit to provide good solubility for improved film quality in OLEDs. It is important to note that the EQE of IDSe-4F and IDSe-4Cl is sevenfold higher than that of its molecular analogue TTT-C20-4F (~0.017%, **Table 1**), highlighting the importance of retarding high-frequency vibration modes by heavy atom substitution.

The superior device performance is also evident in the current density-radiance-voltage (*J-R-V*) characteristics as shown in **Fig. 4b** where the current density and radiance values increase exponentially by orders of magnitude after turn-on, reaching very high radiances of 12.2 W sr^{-1} m^{-2} at 3.6 V in the IDSe-4F device and 12.4 W sr^{-1} m^{-2} at 4.2 V in the IDSe-4Cl device, respectively. The encouraging radiance values

correspond to high radiant exitance (irradiance) of 3.8-3.9 mW cm^{-2} (corresponding to 0.07 sun direct sunlight infrared irradiance that is 51 mW cm^{-2}), which is a dramatic enhancement by 60-fold as compared to that of the best-reported organic emitter with similar EL spectra[3] and the brightest SWIR OLEDs to date (**Supplementary Table 2** and **Supplementary Fig. 9**). Interestingly, the turn-on voltage (V_{on}, the voltage at which radiance of 1 mW sr^{-1} m^{-2} is detected) of the IDSe-4F and IDSe-4Cl devices is as low as 1.02±0.076 V and 0.95±0.055 V, respectively, which is essentially below the nominal emitted photon voltage (~1.1 V, defined by $V_{ph}= hv/e$, where hv is the emitted photon energy). The EL emission at subgap voltages is also observed in other A-D-A type NIR/SWIR emitters (**Table 1** and **Supplementary Fig. 8**), among which, the COTIC-4F device achieved a V_{on} of (0.78±0.041) V, which is obviously lower than the V_{ph} of 1.14 V and is the lowest reported one in the whole OLEDs field so far.

Due to thermodynamic constraints, EL emission at voltages below emitted photon energy is hardly ever accessible but can occur without violating the energy conservation law through the recombination of diffusion-driven and thermally generated charge carriers[46]. Under any voltage above 0 V, diffusion current due to the gradient of the carrier concentrations starts to flow, following an exponential dependence on the applied voltage. According to the mechanism, it was demonstrated that once charge recombination is dominated by the diffusion of charge carriers, rather than by drift current, while accumulation of majority carriers takes place at the same time, emissive Langevin recombination can become apparent even when at subgap voltages. In our devices, the barrier-free hole injection into the emissive layer leads to hole accumulation at the active layer/cathode interface, while relatively small built-in potential gives rise to establishment of a positive drift current at low-forward bias (**Supplementary Fig. 10**). It is equally important to note that the recombination

$R = \gamma N_C^2 e^{-\frac{E_g}{k_B T}} \left(e^{\frac{eV}{k_B T}} - 1 \right)$, where γ is the bimolecular recombination coefficient, N_C the the effective density of states in the conduction band, and k_B Boltzmann's constant. Therefore, the recombination rate in our low bandgap devices is sufficiently high to fulfill the condition for diffusion-dominated recombination occurring, leading to the EL emission at subgap voltages.

It is noteworthy that all devices can operate up to high current density of 2000-3000 mA cm^{-2} (**Fig. 4c** and **Supplementary Fig. 8**), which is challenging to realize in previous NIR/SWIR OLEDs. Moreover, this high current density corresponds to a carrier density of around 10^{18} cm^{-3}, a threshold for lasing under electrical excitation[47]. Interestingly, with increasing current density, the EQE values for all devices except those based on larger bandgap (*e.g.*, Y11 and i-IDSe-4Cl) demonstrate a significant increase, which ultimately gives rise to high SWIR radiance. This EQE dependency on current density is particularly striking, as it implies that the radiative recombination can compete with non-radiative recombination at high current density in the OLEDs. One possible interpretation for this unusual dependency is that it corresponds to a trap-filling process with increasing voltage that not only shifts the recombination zone away from the electrode but also eliminates the non-radiative trap-assisted recombination, leading to an EQE enhancement of more than a factor of two in most devices. The injection-dependent EL spectra shown in **Supplementary Fig. 11** is consistent with a recent study by Blom *et al.* who reported a voltage-dependent EL is a fingerprint of trap-assisted recombination[48], thus confirms the interpretation of radiative recombination dominates over competing trap-assisted recombination with increasing current density. In these ways, the A-D-A type organic

semiconductors possess the potential to fundamentally overcome the SWIR lasing boundary set by the high excitation threshold requirement and efficiency roll-off at high current density.

To demonstrate the potential of our technology, we fabricated large area SWIR OLEDs based on IDSe-4Cl/IDSe-4F. **Fig. 4d** displays a photograph of a typical IDSe-4Cl device with peak emission wavelength at 1110 nm and SWIR radiation power of ~0.6 mW at a current density of 22 mA cm^{-2}, showing remarkable emission uniformity over the substrate area with size of 15 × 15 mm^2. The large area device possesses high maximum SWIR output power of ~8.8 mW, which is comparable to 10 mW for InGaAs-based LEDs. These results would be promising to our devices as cost-efficiency flat-panel light source for applications in portable spectrometer, information-secured displays, night-vision target identification. To provide visualization for these applications, we set up an optical wireless communication system (**see Methods** for the setup and **Fig. 4e** for the simplified block diagram), in which our SWIR OLEDs are integrated as the transmitter for free space data link. Transmitting audio signals or pulse signals is achieved through modulation of infrared light, while an InGaAs photodiode was used as receiver for audio signal recovery. As shown in **Fig. 4e**, there is no obvious distortion in the received signals, indicating our system provides sufficient transmission capacity. Due to the bright radiance and the fast switching ability, the application of our SWIR OLEDs makes light fidelity (Li-Fi) communication possible and more flexible. We further demonstrate real-time through-biological-tissue (*e. g.* meat and fish slice) audio signals and pulsed signals transmission (**Supplementary Videos 1-2**). In contrast, the signal propagation is blocked in a visible light communication system in which saturated red LEDs peaked at 630 nm is employed as transmitter (**Supplementary Video 3**). We further

demonstrate that SWIR OLEDs have held great promise for semiconductor wafer and chip quality inspection. Since the absorption edge is ~1100 nm for multi-crystalline Si and ~1050 nm single-crystalline, our IDSe-4Cl device is more advantageous in that its emission peak located at 1110 nm as compared to visible light source. Indeed, as shown in **Fig. 4f**, the SWIR light sources exhibit considerable optical transmission, while the wafer is opaque to the visible light source. The emission from the IDSe-4Cl OLEDs can penetrates the wafer from bottom to top and reveal more details, making them ideal for industrial applications, such as pinholes and cracks detection in wafer. Snapshot images of microchip yielded by SWIR irradiance from our devices is shown in **Fig. 4g**, with the images obtained from visible light illumination included for comparison. The details of microcircuit details and defects or crack can be clearly observed in the SWIR image, while part of visible image is obscure. In addition, the device exhibits good operation stability, with an operation lifetime of at least 1000 h at a high current density of 100 mA cm^{-2} (**Supplementary Fig. 12**). These findings on large area devices with high brightness and good stability open up the pathway toward low-cost, portable SWIR OLEDs light sources for emerging applications.

Conclusion

In summary, we demonstrate organic light-emitting devices (OLEDs) with bright SWIR emission by using finely tuned acceptor-donor-acceptor (A-D-A) type molecules as emitters. The resultant OLEDs exhibited unprecedented device performance values, including the highest radiance and efficiency in SWIR region, unprecedentedly low turn-on voltage at subgap voltages and even higher efficiency at high current density on the order of ~A cm^{-2}. We found that the impressive performances of these SWIR OLEDs are essentially due to the excellent

photophysical properties of the A-D-A type molecules, in which co-planarity, rigidity of π-conjugated backbones, extremely small reorganization energy and electron-phonon coupling factor, combined with heavy atom substitution that retard high-frequency vibration modes, contributed to significantly suppressed non-radiative recombination rate and improved PLQY. Furthermore, given the large oscillator strength and the ability to operate at high current density, these A-D-A type molecules hold the potential to fulfill electrically pumped SWIR laser. Benefiting from the semi-transparency of biological tissue to SWIR radiation, the high radiation power, together with the absence of toxic heavy metals, our devices provide a promising outlook for a wide range of emerging applications (**Supplementary Fig. 13**), such as next-generation optoelectronic devices, wearable biosensors, implantable bioelectronics, internet of things (IoT) connectivity and biological imaging.

Online content

Any methods, additional references, Nature Research reporting summaries, source data, extended data, supplementary information, acknowledgements, peer review information; details of author contributions and competing interests; and statements of data and code availability are available online.

References

1. Tang, C. W. & VanSlyke, S. A. Organic electroluminescent diodes. *Appl. Phys. Lett.* **51**, 913–915 (1987).

2. Burroughes, J. H. *et al.* Light-emitting diodes based on conjugated polymers. *Nature* **347**, 539–541 (1990).

3. Qian, G., Zhong, Z., Luo, M., Yu, D., Zhang, Z.,Wang, Z. Y. & Ma, D. *Adv. Mater.*

21, 111–116 (2009).

4. Zampetti, A., Minotto, A. & Cacialli, F. Near-infrared (NIR) organic light-emitting diodes (OLEDs): challenges and opportunities. *Adv. Func. Mater.* **29**, 1807623 (2019).

5. Zheng, Y. & Zhu, X. Recent progress in emerging near-infrared emitting materials for light-emitting diode applications. *Org. Mater.* **2**, 253–281 (2020).

6. Konstantatos, G. *et al.*. Ultrasensitive solution-cast quantum dot photodetectors. *Nature* **442**, 180−183 (2006).

7. Lu, H., Carroll, G. M., Neale, N. R. & Beard, M. C., Infrared quantum dots: progress, challenges, and opportunities. *ACS Nano* **13**, 939−953 (2019).

8. Murphy, C. J. Optical sensing with quantum dots. *Anal. Chem.* **74**, 520A–526A (2002).

9. Smith, A. M., Mancini, M. C. & Nie, S. Second window for in vivo imaging. *Nat. Nanotechnol*. **4**, 710−711 (2009).

10. Wilson, R. H., Nadeau, K. P., Jaworski, F. B., Tromberg, B. J. & Durkin, A. J. Review of short-wave infrared spectroscopy and imaging methods for biological tissue characterization. *J. Biomed. Opt.* **20**, 030901 (2015).

11. Diao, S., Blackburn, J. L., Hong, G., Antaris, A. L., Chang, J., Wu, J. Z., Zhang, B., Cheng, K., Kuo, C. J. & Dai, H. Fluorescence imaging in vivo at wavelengths beyond 1,500 nm. *Angew. Chem., Int. Ed.* **54**, 14758−14762 (2015).

12. Bruns, O. T. *et al*. Next-generation in vivo optical imaging with short-wave infrared quantum dots. *Nat. Biomed. Eng.* **1**, 0056 (2017).

13. Minotto, A. *et al.* Towards efficient near-infrared fluorescent organic light-emitting diodes. *Light Sci. Appl.* **10**, 18–27 (2021).

14. Wu, J. When group-III nitrides go infrared: New properties and perspectives. *J.*

Appl. Phys. **106**, 011101 (2009).

15. Tessler, N., Medvedev, V., Kazes, M., Kan, S. & Banin, U. Efficient near-infrared polymer nanocrystal light-Emitting diodes. *Science* **295**, 1506–1508 (2002).
16. Qi, J., Qiao, W. & Wang, Z. Y. Advances in organic near-infrared materials and emerging applications, *Chem. Rec.* **16**, 1531–1548 (2016).
17. Ho, C. L., Li, H. & Wong, W. Y. Red to near-infrared organometallic phosphorescent dyes for OLED applications. *J. Organomet. Chem.* **751**, 261–285 (2014).
18. Ai, X., Evans, E. W., Dong, S., Gillett, A. J., Guo, H., Chen, Y., Hele, T. J. H., Friend, R. H., Li, F. Efficient radical-based light-emitting diodes with doublet emission, *Nature* **563**, 536–540 (2018).
19. Tao, R., Qiao, J., Zhang, G., Duan, L., Chen, C., Wang, L. & Qiu, Y. High-efficiency near-infrared organic light-emitting devices based on an iridium complex with negligible efficiency roll-off. *J. Mater. Chem. C* **1**, 6446–6454 (2013).
20. Wei, Y. C. *et al.* Overcoming the energy gap law in near-infrared OLEDs by exciton–vibration decoupling. *Nat. Photon.* **14**, 570–577 (2020).
21. Suzuki, H. Infrared electroluminescence from an organic ionic dye containing no rare-earth ions. *Appl. Phys. Lett.* **80**, 3256–3258 (2002).
22. Chen, .M, Perzon, E., Andersson, M. R., Marcinkevicius, S., Jönsson. S. K. M., Fahlman, M. & Berggren, M. 1 micron wavelength photo- and electroluminescence from a conjugated polymer. *Appl. Phys. Lett.* **84**, 3570–3572 (2004).
23. Minotto, A., Murto, P., Genene, Z., Zampetti, A., Carnicella, G., Mammo, W.,

Andersson, M. R., Wang, E. & Cacialli, F. *Adv. Mater.* **30**, 1706584 (2018).

24. Qian, G., Dai, B., Luo, M., Yu, D., Zhan, J., Zhang, Z., Ma, D. & Wang, Z. Y. Band gap tunable, donor-acceptor-donor charge-transfer heteroquinoid-based chromophores: near infrared photoluminescence and electroluminescence, *Chem. Mater.* **20**, 6208–6216 (2008).
25. Yao, L., Zhang, S., Wang, R., Li, W., Shen, F., Yang, B. & Ma, Y. Highly efficient near-infrared organic light-emitting diode based on a butterfly-shaped donor–acceptor chromophore with strong solid-state fluorescence and a large proportion of radiative excitons, *Angew. Chem. Int. Ed.* **53**, 2119–2123 (2014).
26. Kim, D. H. *et al*. High efficiency electroluminescence and amplified spontaneous emission from a thermally activated delayed fluorescent near-infrared emitter. *Nat. Photon.* **12**, 98–104 (2018).
27. Yu, Y. *et al*. Near-infrared electroluminescence beyond 800 nm with high efficiency and radiance from anthracene cored emitters. *Angew. Chem. Int. Ed.* **59**, 21578–21584 (2020).
28. Tregnago, G., Steckler, T.T., Fenwick O., Andersson, M. R. & Cacialli, F. Thia- and selenadiazole containing polymers for near-infrared light-emitting diodes. *J Mater. Chem C* **3**, 2792–2797 (2015).
29. Lin, Y., Wang, J., Zhang, Z.-G., Bai, H., Li, Y., Zhu, D. & Zhan, X. An electron acceptor challenging fullerenes for efficient polymer solar cells. *Adv. Mater.* **27**, 1170−1174 (2015).
30. Liu, S., Yuan, J., Deng, W., Luo, M., Xie, Y., Liang, Q., Zou, Y., He, Z. Wu, H. & Cao, Y. High-efficiency organic solar cells with low non-radiative recombination loss and low energetic disorder. *Nat. Photon.* **14**, 300–305 (2020).
31. Rau, U. Reciprocity relation between photovoltaic quantum efficiency and

electroluminescent emission of solar cells. *Phys. Rev. B* **76**, 085303 (2007).

32. Lee, J. *et al*. Bandgap narrowing in non-fullerene acceptors: single atom substitution leads to high optoelectronic response beyond 1000 nm. *Adv. Energy Mater.* **8**, 1801212 (2018).
33. Roncali, J. Molecular engineering of the band gap of π-conjugated systems: facing technological applications. *Macromol. Rapid Commun.* **28**, 1761–1775 (2007).
34. Shuai, Z. G. & Peng, Q. Organic light-emitting diodes: theoretical understanding of highly efficient materials and development of computational methodology. *Natl. Sci. Rev*. **4**, 224–239 (2017).
35. Benduhn, J. *et al.* Intrinsic non-radiative voltage losses in fullerene-based organic solar cells. *Nat. Energy* **2**, 17053 (2017).
36. Perdigón-Toro, L. *et al.* Excitons dominate the emission from PM6:Y6 solar cells, but this does not help the open-circuit voltage of the device. *ACS Energy Lett.* **6**, 557–564 (2021).
37. Jortner, J. Temperature dependent activation energy for electron transfer between biological molecules. *J. Chem. Phys.* **64**, 4860–4867 (1976).
38. Gould, I. R. *et al.* Radiative and nonradiative electron transfer in contact radical-ion pairs. *Chem. Phys.* **176**, 439–456 (1993).
39. Azzouzi, M. *et al.* Nonradiative energy losses in bulk-heterojunction organic photovoltaics. *Phys. Rev. X* **8**, 031055 (2018).
40. Wilson, J. S. *et al.* The energy gap law for triplet states in Pt-containing conjugated polymers and monomers. *J. Am. Chem. Soc.* **123**, 9412–9417 (2001).
41. Cave, R. J. & Newton, M. D. Generalization of the Mulliken-Hush treatment for the calculation of electron transfer matrix elements. *Chem. Phys. Lett.* **249**, 15–19 (1996).

42. Zhu, W. *et al*. Crystallography, morphology, electronic structure, and transport in non-fullerene/non-Indacenodithienothiophene polymer: Y6 solar cells. *J. Am. Chem. Soc.* **142**, 14532–14547 (2020).

43. Zhang, G. *et al*. Delocalization of exciton and electron wavefunction in non-fullerene acceptor molecules enables efficient organic solar cells. *Nat. Commun 11,* 3943 (2020).

44. Yao, H., Cui, Y., Yu, R., Gao, B., Zhang, H., Hou, J. Design, synthesis, and photovoltaic characterization of a small molecular acceptor with an ultra-Narrow band gap. *Angew. Chem., Int. Ed.* **56**, 3045−3049 (2017).

45. Intemann, J. J. *et al*. Molecular weight effect on the absorption, charge carrier mobility, and photovoltaic performance of an indacenodiselenophene-based ladder-type polymer. *Chem. Mater.* **25**, 3188–3195 (2013).

46. Li, Y., Sachnik, O., Van der Zee, B., Thakur, K., Ramanan, C., Wetzelaer, G. J. A., & Blom, P. W. Universal electroluminescence at voltages below the energy gap in organic light-emitting diodes. *Adv. Optical Mater.* **8**, 2101149 (2021).

47. Liu, X. K., Xu, W., Bai, S., Jin, Y., Wang, J., Friend, R. H. & Gao, F. Metal halide perovskites for light-emitting diodes. *Nat. Mater*. **20**, 10–21 (2021).

48. Kuik, M. *et al*. 25th Anniversary Article: Charge transport and recombination in polymer light-emitting diodes. *Adv. Mater*. **26**, 512–531 (2014).

Methods

Materials

A-D-A type molecules Y11, SiOTIC-4F and COTIC-4F were obtained as commercial chemicals from 1-Material Inc, Y6 and BTA 3 were purchased from Solarmer Inc. Perylene diimide functionalized with amino N-oxide (PDINO) was purchased from Sigma-Aldrich. Poly(3,4-ethylenedioxythiophene) polystyrene sulfonate (PEDOT: PSS) in aqueous solution was purchased from H. C. Starck. All purchased chemicals were used as received without additional purification. Unless otherwise stated, all other A-D-A type molecules were synthesized in the laboratory by a route described in **Supplementary Methods**.

Computational methods

The initial geometries of these three molecules were optimized with the range-separated functional ωB97XD (with a default range-separation parameter ω of 0.2 $bohr^{-1}$) and the 6-31G(d,p) basis set. Then, following our earlier works [26, 49], an iteration procedure was used to non-empirically tune the ω parameter with the implicit consideration of the dielectric environment via the polarisable continuum model (PCM); the dielectric constant ε was chosen to be 4.5, a representative value of nonpolar organic semiconductor materials. Time-dependent density functional theory (TD-DFT) was employed to study the excited-state properties. All quantum-chemical calculations were performed with the Gaussian 16 Rev A03 program[50]. The overlaps between the NTO electron and hole wavefunctions describing the S_1 excited states were quantified by using Multiwfn program[51].

Optical absorption and photoluminescence characterization

The absorption spectra of the solid-state films were measured with a UV-vis-NIR spectrophotometer (UV3600, SHIMADZU). For the steady-state photoluminescence measurement, semiconductor lasers were used as excitation and the wavelength was 530 nm for $PC_{71}BM$, or 635 nm (for BTA3, ITIC, IT-M, IT-4F and i-IEICO-4F) or 852 nm (for Y6, Y11, IDSe-(Th, 4F, and 4Cl), SiOTIC-4F and COTIC-4F). Calibrated spectrometers (QE Pro and NIR Quest 512, Ocean Optics) equipped with cooled Hamamatsu CCD array (-20 ℃) in conjunction with an integrated sphere severed as the spectral acquisition system. To minimize the scattering of incident laser, long pass filters with cutoff wavelength at 750 nm or 860 nm was placed between the samples and detector.

Photoluminescence quantum yield measurements

The absolute PLQY for emitters with emission between 300 nm and 950 nm were measured using integrating sphere coupled spectrometer (QEPro, Ocean Optics) and further verified by a commercial absolute PLQY measurement system (C11347-11, Hamamatsu Photonics), while PLQY for emission above 950 nm was determined with an integrating sphere and a calibrated spectrometers (NIR Quest 512, Ocean Optics), as the ratio of the number of photons re-emitted to the number of photons absorbed.

Time-resolved photoluminescence spectra measurements

The time-resolved photoluminescence spectra of the emitters were acquired using a fluorescence lifetime spectrometer by means of a time-correlated single-photon-counting (TCSPC) technique (Hydraharp 400, PicoQuant). The samples were excited by a femtosecond Ti: Sapphire-pulsed laser from Coherent Inc. with pulse duration of 120 fs, a fluence of ~0.2 μJ cm^{-2} per pulse and a repetition rate of 80 MHz. The photoluminescence data were collected using a single-photon-counting photomultiplier tube detector. Long pass filters with cutoff wavelength at 715 nm or 780 nm was placed before the detector to minimize the scattering of incident laser.

Device fabrication and characterization

Device fabrication. The devices were fabricated on patterned indium tin oxide (ITO)-coated glass substrates with a sheet resistance of 15–20 ohm per square. ITO substrates had underwent a series of wet-cleaning course in an ultrasonic bath, beginning with acetone, followed by deionized water and isopropanol, finally dried in the oven over night. After air-plasma treatment, a 40 nm-thick poly(3,4-ethylenedioxythiophene) polystyrene sulfonate (PEDOT: PSS 4083) anode buffer layer was spin-cast on the precleaned ITO substrate then dried by baking at 150 °C for 20 min. Subsequently, the luminescent small molecule films (COTIC-4F, IDSe-4Cl and Y11 etc.) were prepared by spin-coating their chloroform solution (with a concentration of 20 mg ml^{-1}) at 2000 r. p. m. for 30 s to form a uniform 100 nm-thick film on the top of anode buffer layer. Then a 10 nm-thick perylene-diimide derivative (PDINO) layer was deposited onto the emitting layer by spin-coating from

methanol solution (with a concentration of 1.5 mg ml^{-1}). Finally, 100 nm-thick silver electrode was evaporated with a shadow mask (~2×8 mm^2) in a vacuum chamber with a pressure of 1×10^{-4} Pa. All the device fabrication process, except for the spin-coating of PEDOT: PSS layer, were carried out in a nitrogen filled glove box (O_2< 1 ppm, H_2O< 1 ppm) without exposure to air. We fabricated devices for each emitter at least four times under similar conditions and evaluated at least 15 devices for each emitter reported. Before measurements, the fabricated devices were encapsulated using a cover glass plate and an ultraviolet cured epoxy resin.

Current density-Radiance-Voltage (J–R-V) characteristics and external quantum efficiency measurements. Current density-Voltage characteristics of devices were measured using a Keithley 238 source-meter unit, while radiance-voltage characteristics were simultaneously recorded using a silicon photodiode. The radiance of electroluminescence was calibrated with an infrared spectrometer (NIRQuest512, Ocean Optics) by collecting the emitting photons in all directions through an integrated sphere. The InGaAs detector of the spectrometer is calibrated from 900 nm to 1700 nm, by a standard halogen calibration light source (HL-3-plus-INT-CAL), of which the wavelength of irradiance ranges from 350 nm to 2400 nm. EQE is calculated through dividing the number of photons extracted by the number of electrons injected, per unit time.

Electroluminescence spectroscopy measurements. EL spectra for devices with emission peaks between 700 nm and 1000 nm were recorded using spectrometer (QEPro, Ocean Optics) with calibrated a silicon photodetector. EL spectra for devices with emission peaks past 1000 nm were recorded using a spectrometer (NIRQuest512, Ocean Optics) equipped with InGaAs line photodetector (calibrated from 900 nm to 1700 nm).

Operational Lifetime measurement. Before the operational lifetime measurement, devices were stored in a nitrogen-filled glove box in dark. The operational lifetime of the devices was evaluated using a home-made operational lifetime measurement equipped with silicon photodiode under constant current stress condition, which was calibrated by a spectrometer (NIRQuest512, Ocean Optics).

Setup of optical wireless communication system

A transistor (Model: S9013) is used to obtain audio signal amplification and drive SWIR OLEDs for analogue audio signal transmission. At the receiver end, a high sensitivity InGaAs photodetector (MTPD1346D-300) is employed to convert radiation into photocurrent, which is transmitted to a speaker trough a low voltage audio power amplifier (LM386). For the transmission of pulsed signal, the signal was produced by a function generator (AFG3102C, Tektronix), the transmitted and received signal were displayed by an oscilloscope (MDO3024, Tektronix) via two independent channels.

SWIR photographs and videos

Photographs and videos of SWIR light source were taken using SWIR camera (LD-SW6401725-CTE2-G from Leading Optoelectronic Inc or ARTCAM-032 from Artray Inc) whose detection range was between 950-1700 nm with the pixel resolution of 25 μm. Microscopic photographs were taken by transflective polarizing microscope (XP4A, SHMLT) equipped with a visible charge-coupled device (CCD), the SWIR photographs were recorded by switching the self-equipped CCD to SWIR camera.

Data availability

The data that support the findings of this study are available from the corresponding author upon reasonable request.

References

49. Cui, L.-S. *et al.* Fast spin-flip enables efficient and stable organic electroluminescence from charge-transfer states. *Nat. Photon.* **14**, 636–642 (2020).

50. Frisch, M. J. *et al.* Gaussian 16, revision C.01 (Gaussian, Inc., 2016).

51. Lu, T. & Chen, F. Multiwfn: A multifunctional wavefunction analyzer. *J. Comput. Chem*. **33**, 580–592 (2012).

Acknowledgements

H.W. thanks the National Natural Science Foundation of China (No. 51521002) for financial support. Y. X. acknowledges the National Natural Science Foundation of China (No. 52003087) for financial support. C. G. thanks the Shaanxi Key Scientific and Technological Innovation Team Project (No. 2016KCT-28), and Shaanxi Key Project in Industrial Field (No. 2017ZDXM-GY-046) for financial support. W. D. acknowledges support from the National Natural Science Foundation of China (No. 62004069). X.-K.C. acknowledges the New Faculty Start-up Grant of the City University of Hong Kong (7200709, 9610547).

Author contributions

Y.X., H.W. and C. G. conceived the idea. Y.X. and W.L. fabricated the SWIR OLEDs devices. C.G., H.-M. W. and W.W. designed and synthesized the i-IDSe- and IDSe-series A-D-A type emitters. Y.X. performed the numerical simulations. X.-K. C. performed the theoretical calculations and provided feedback on the manuscript. Y. X., W.L. and W.D. performed the device characterization and optical absorption measurements. W. D. and W. L. performed the time-resolved photoluminescence decay measurements. Y.X. and W.D. performed the recombination rate calculations. W.L. and Y.X. acquired the SWIR EL photographs. Y.S. set up the optical communication system. W.L. and Y.X. carried out optical communication demonstration, wafer quality inspection and operational lifetime tests. X.Z. and J.P. discussed the results and commented on the manuscript. H.W., Y. X., C. G., W. D., W. L. and X.C. contributed to the writing of the manuscript. All authors discussed the experiments and results. H. W, C. G. and Y. C. supervised the project and advised on device optimization.

Competing interests The authors declare no competing interests.

Additional information

Supplementary information is available for this paper online.

Correspondence and requests for materials should be addressed to Y. X, C. G., X.-K.C. or H. W.

Reprints and permissions information is available at http://www.nature.com/reprints.

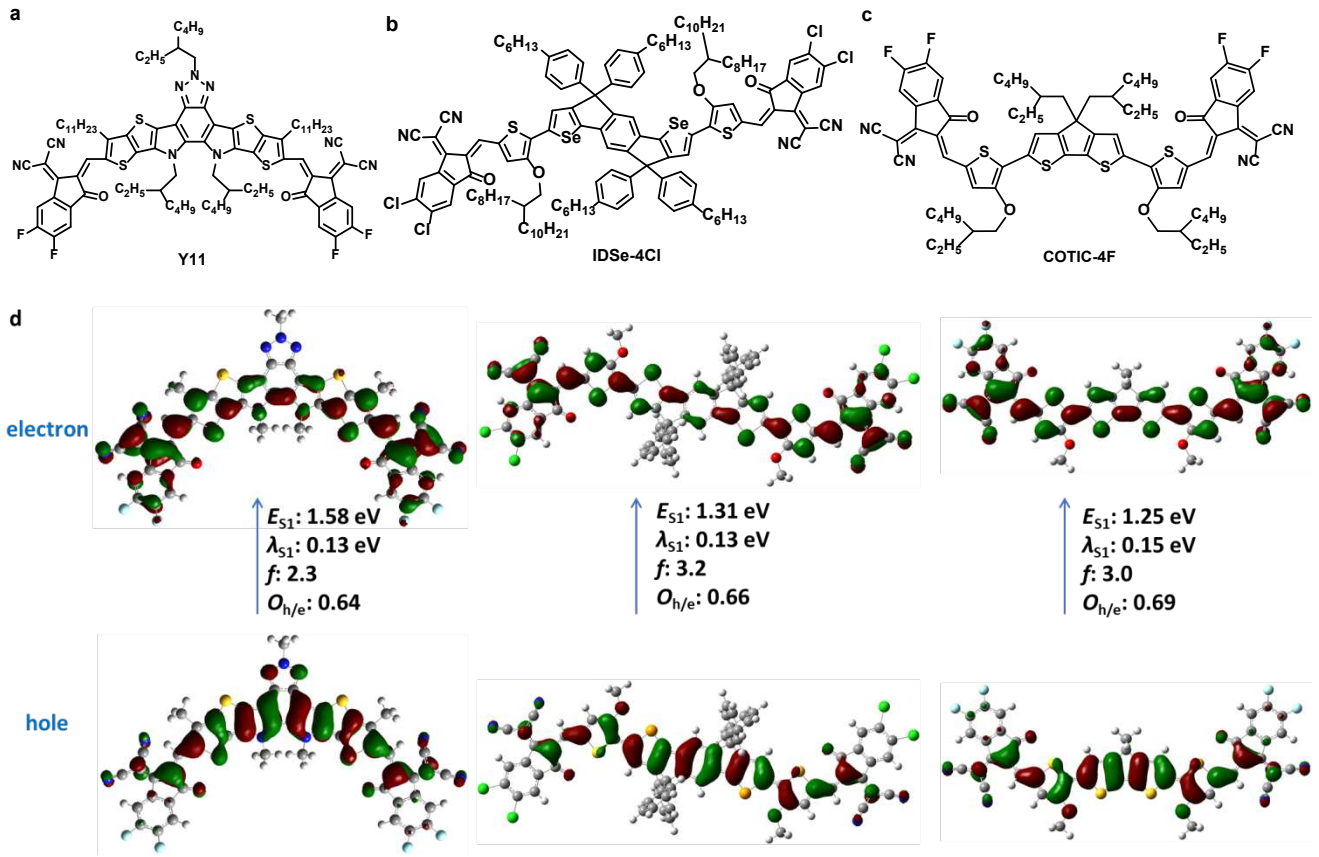

Figure 1 | Chemical structures and theoretical calculation results. **a–c**, Molecular structures of representative SWIR emitting organic molecules studied in this work. **d**, Natural transition orbitals (NTO: hole and electron), adiabatic excited-state energies (E_{S1}), total reorganization energies ($\lambda_{S1}= \lambda_S + \lambda_v$) including the two parts due to the low-frequency and high-frequency vibrations, oscillator strengths (f), and overlap

between NTO electron and hole orbitals ($O_{h/e}$) for the first singlet (S_1) excited states of Y11, IDSe-4Cl and COTIC-4F, calculated via ωB97XD/6-31G(d,p) with the optimally tuned ω parameters.

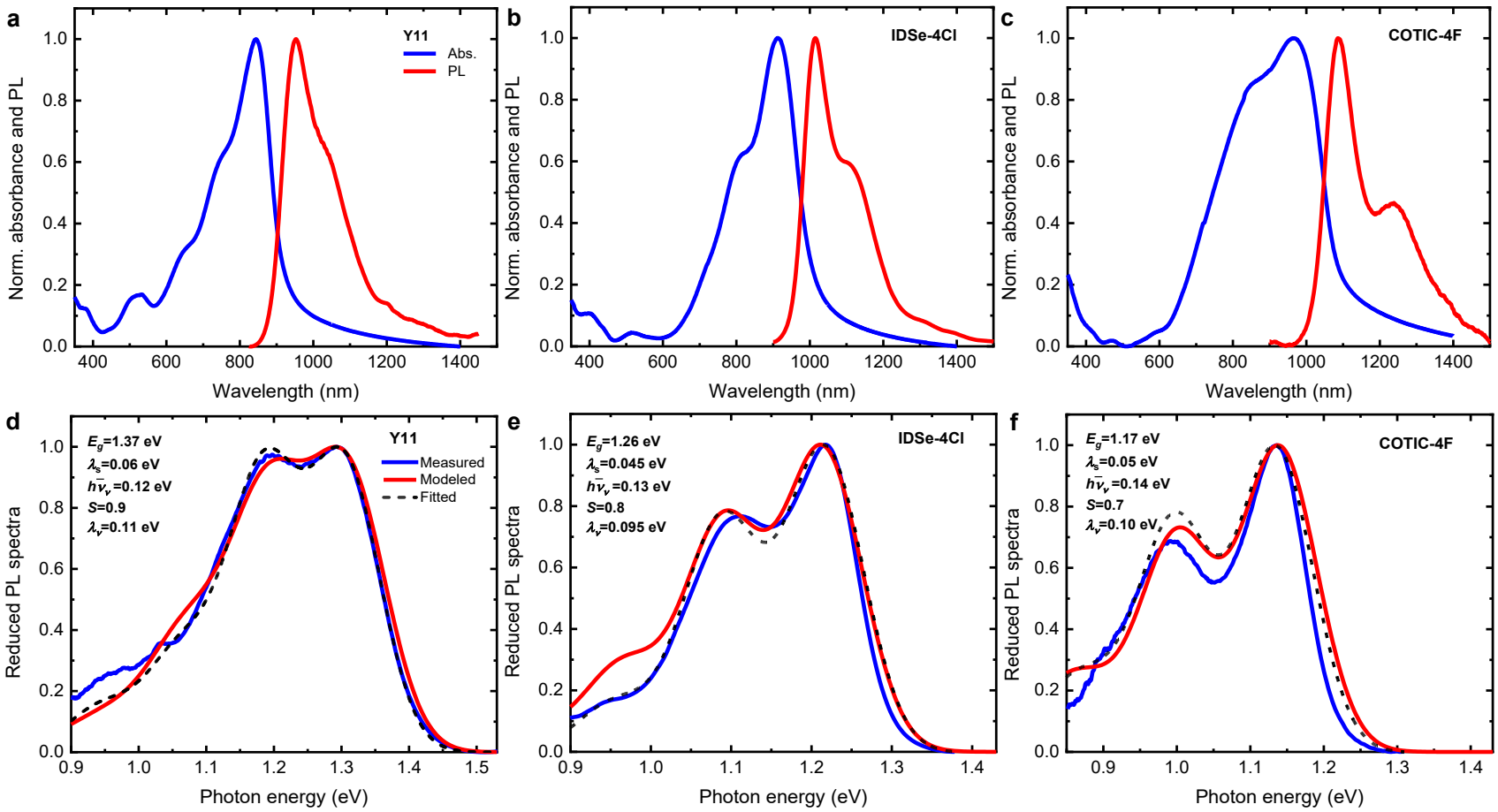
a
Y11
Abs.
PL
Norm. absorbance and PL
Wavelength (nm)
b
IDSe-4Cl
Norm. absorbance and PL
Wavelength (nm)
c
COTIC-4F
Norm. absorbance and PL
Wavelength (nm)
d
Y11
E_g=1.37 eV
λ_s=0.06 eV
$h\bar{\nu}_v$=0.12 eV
S=0.9
λ_v=0.11 eV
Measured
Modeled
Fitted
Reduced PL spectra
Photon energy (eV)
e
IDSe-4Cl
E_g=1.26 eV
λ_s=0.045 eV
$h\bar{\nu}_v$=0.13 eV
S=0.8
λ_v=0.095 eV
Reduced PL spectra
Photon energy (eV)
f
COTIC-4F
E_g=1.17 eV
λ_s=0.05 eV
$h\bar{\nu}_v$=0.14 eV
S=0.7
λ_v=0.10 eV
Reduced PL spectra
Photon energy (eV)

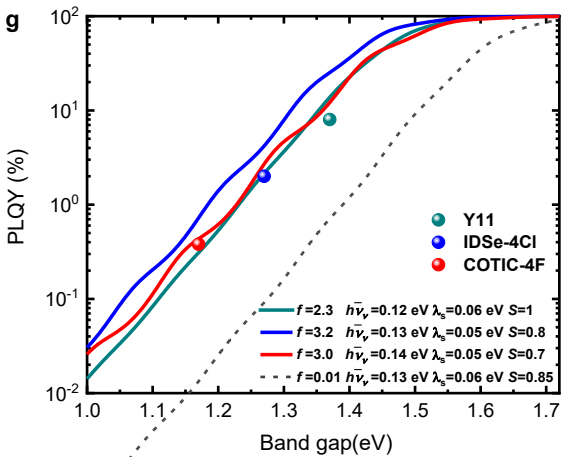

Figure 2 | Optical properties and photophysical studies of representative A-D-A molecules. a–c, The absorption and photoluminescence spectra of the SWIR emitters in solid film. **d–f**, Normalized reduced emissions deduced from the measured photoluminescence through Equation (1) and the corresponding curves fitted by multiple Gaussian peaks, the emission spectra modeled by Equation (2) with the extracted parameters as input are also shown. **g**, The modeled PLQYs with specific photophysical parameters extracted from Y11, IDSe-4Cl and COTIC-4F are plotted as a function of optical gap, their experimentally measured PLQYs are shown as scattered dots for comparison.

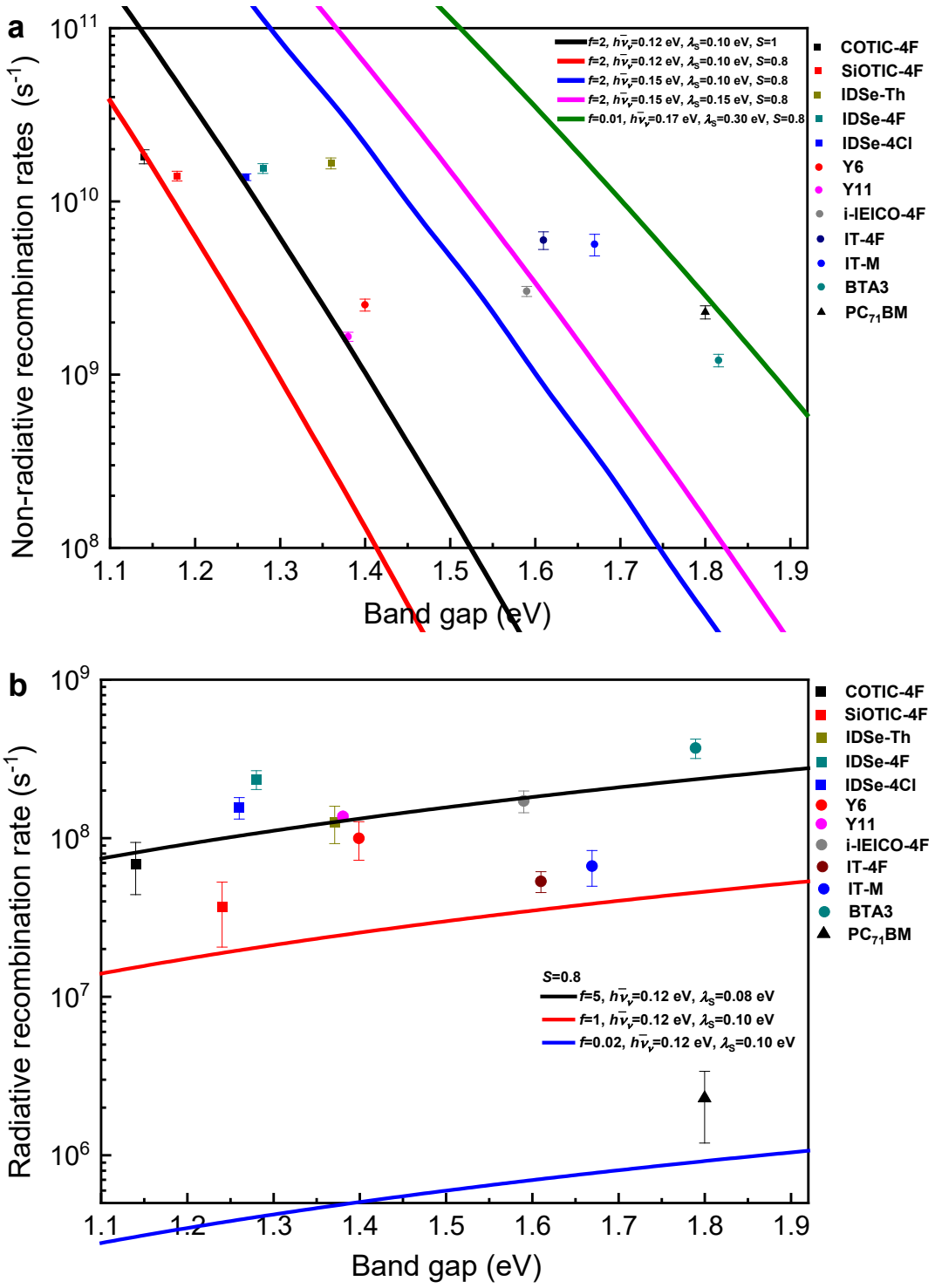
a
Non-radiative recombination rates (s-1)
Band gap (eV)
f=2, hν̄v=0.12 eV, λS=0.10 eV, S=1
f=2, hν̄v=0.12 eV, λS=0.10 eV, S=0.8
f=2, hν̄v=0.15 eV, λS=0.10 eV, S=0.8
f=2, hν̄v=0.15 eV, λS=0.15 eV, S=0.8
f=0.01, hν̄v=0.17 eV, λS=0.30 eV, S=0.8
COTIC-4F
SiOTIC-4F
IDSe-Th
IDSe-4F
IDSe-4Cl
Y6
Y11
i-IEICO-4F
IT-4F
IT-M
BTA3
PC71BM
b
Radiative recombination rate (s-1)
Band gap (eV)
S=0.8
f=5, hν̄v=0.12 eV, λS=0.08 eV
f=1, hν̄v=0.12 eV, λS=0.10 eV
f=0.02, hν̄v=0.12 eV, λS=0.10 eV
COTIC-4F
SiOTIC-4F
IDSe-Th
IDSe-4F
IDSe-4Cl
Y6
Y11
i-IEICO-4F
IT-4F
IT-M
BTA3
PC71BM

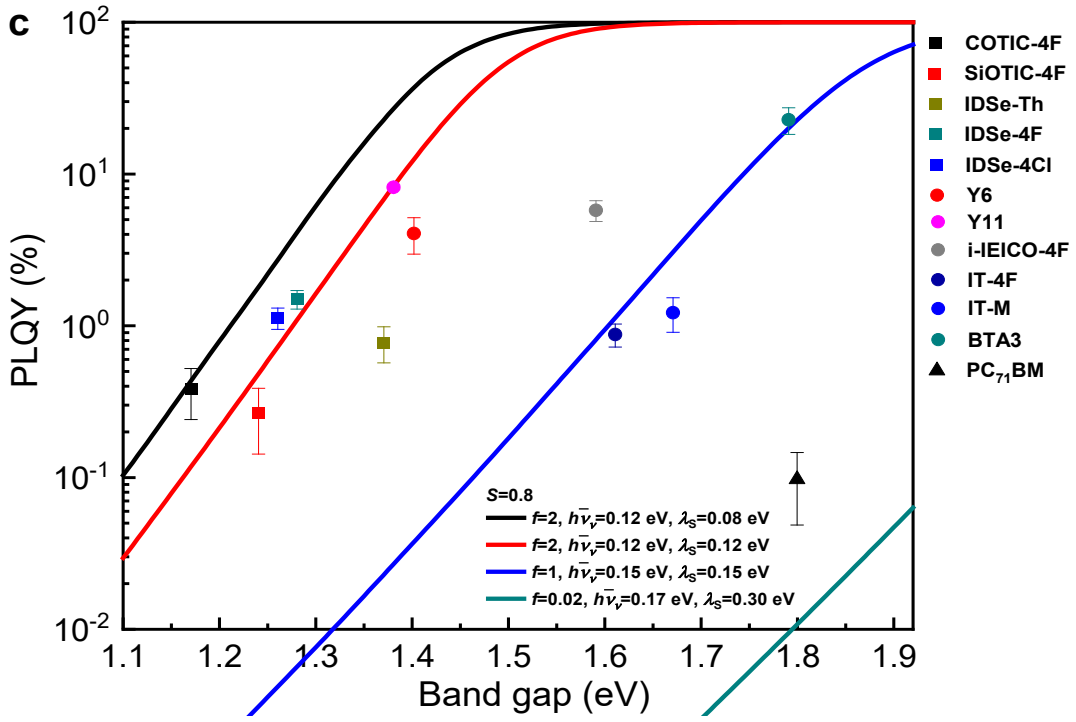

Figure 3 | Rate constants of radiative and non-radiative recombination and photoluminescence quantum yield as well as their correlations with the microscopic parameters. a, Non-radiative recombination rates k_{nr}, **b-c**, Radiative recombination rates k_r (**b**) and PLQY (**c**) as a function of optical bandgap with respect to varied oscillator strength *f*, low-frequency reorganization energy λ_S, mean phonon energy $h\bar{\nu}_v$ andelectron-phonon coupling factor *S*. The scatters are non-radiative and radiative recombination rates extracted from analysis of the time-resolved photoluminescence measurements and PLQY for the materials as $k_{nr} = \frac{1}{\tau} - k_r$ and $k_r = \frac{PLQY}{\tau}$. The error bars represent the standard deviation across six measurements for each emitter.

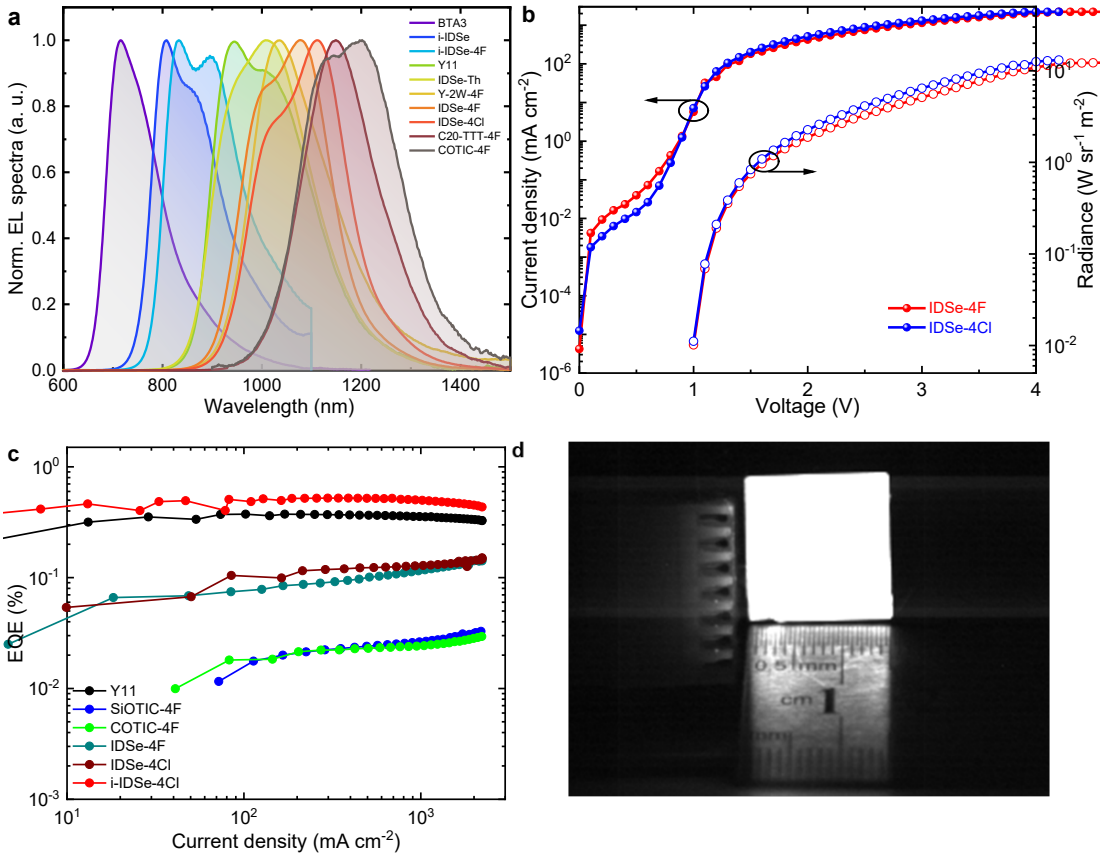
a
Norm. EL spectra (a. u.)
Wavelength (nm)
BTA3
i-IDSe
i-IDSe-4F
Y11
IDSe-Th
Y-2W-4F
IDSe-4F
IDSe-4Cl
C20-TTT-4F
COTIC-4F
b
Current density (mA cm-2)
Radiance (W sr-1 m-2)
Voltage (V)
IDSe-4F
IDSe-4Cl
c
EQE (%)
Current density (mA cm-2)
Y11
SiOTIC-4F
COTIC-4F
IDSe-4F
IDSe-4Cl
i-IDSe-4Cl
d
e
Received Signal
Transmitted Signal
SWIR OLEDs
Setup of optical wireless communication (OWC) System
Driver
SWIR OLEDs
Free space data link
Amplifier
InGaAs PD

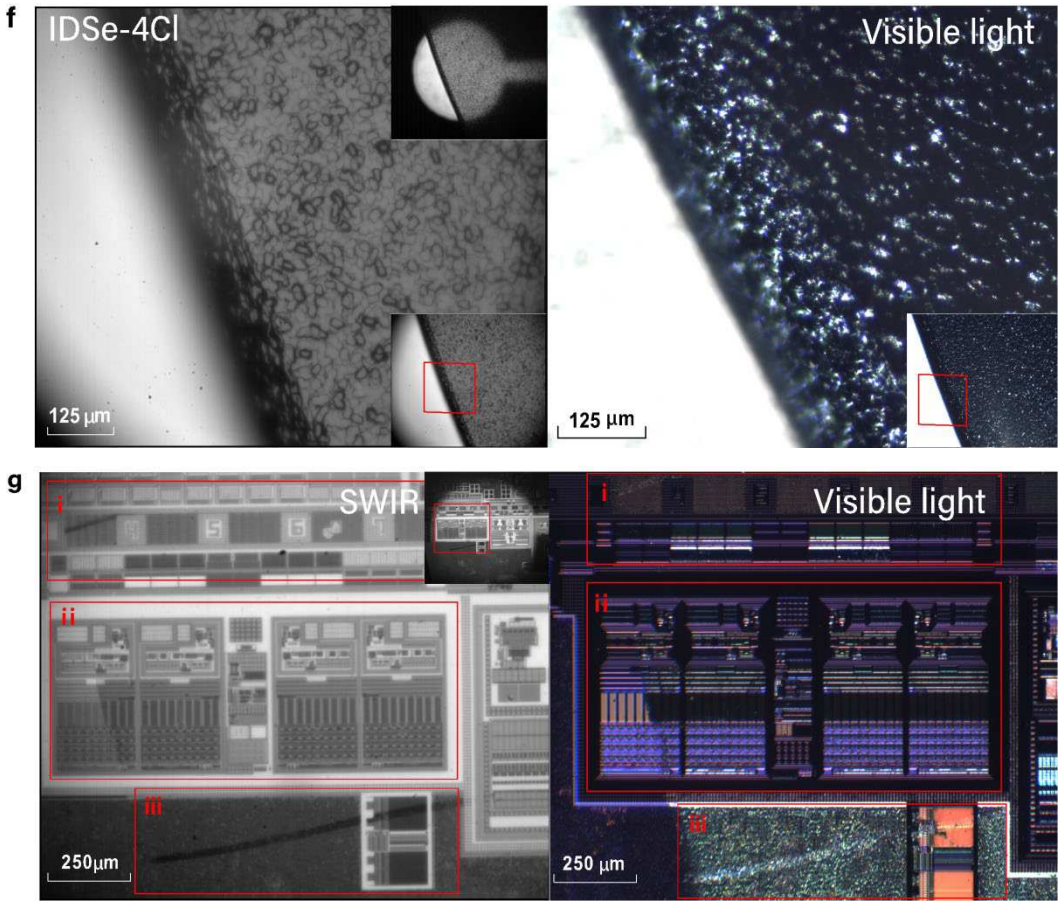
f
IDSe-4Cl
125 µm
Visible light
125 µm
g
SWIR
i
ii
iii
250µm
Visible light
i
ii
iii
250 µm

system are also shown. **f-g,** Demonstration of SWIR OLEDs for applications in semiconductor wafer quality inspection. **f,** Images of a single-sided polished silicon wafer (~250 μm thickness) taken under irradiation of IDSe-4Cl (left panel) and visible light source (right panel). The right top inset in the left panel shows the image of the wafer on top of the SWIR light source at a lower magnification, in which SWIR emission from the bottom penetrates the whole wafer. All SWIR images are taken under transmission mode, while visible images are taken in a reflection mode. **g,** Images of a microchip taken under irradiation of IDSe-4Cl (left panel) and visible (right panel) light source, respectively. Microcircuit areas are marked with i, ii, while defect/crack is mark with iii.

Table 1 | Summary of the SWIR OLEDs performance parameters for the devices investigated in this study.

No.	Emitters	E_g (eV)	0-0 Emission Peak (nm)	0-1 Emission Peak (nm)	PLQY (%)[a]	V_{on} (V)[b]	Max radiance (W sr^{-1} m^{-2}) [b]	Max radiant exitance (mW cm^{-2}) [b]	Maximum EQE (%)[b]
1	BTA3	1.79	720	750	22.8±4.5	1.60±0.05	19.6 (16.6±3.8)	6.16 (5.22±1.20)	0.43 (0.36±0.067)
2	i-IDSe		807	870		1.27±0.082	40.8 (39.0±1.2)	12.7 (12.26±0.38)	0.38 (0.36±0.015)
3	i-IEICO-4F	1.59	810	875	5.73±0.89	1.34±0.073	28.5 (27.1±1.7)	8.95 (8.18±0.50)	0.43 (0.32±0.052)
4	i-IDSe-4F		833	900		1.27±0.051	40.3 (39.0±1.0)	12.6 (12.24±0.31)	0.46 (0.45±0.011)
5	i-IDSe-4Cl		843	920		1.17±0.052	44.8 (44.0±0.53)	14.1 (13.81±0.17)	0.54 (0.53±0.012)
6	Y6	1.4	945	1040	3.97±1.07	1.07±0.075	17.2 (14.2±3.22)	5.4 (4.46±1.01)	0.25 (0.20±0.041)
7	Y11	1.37	945	1035	8.13±0.30	1.01±0.035	27.3 (23.7±4.78)	8.6 (7.96±1.11)	0.33 (0.28±0.070)
8	IDSe-Th	1.37	953	1015	0.75±0.20	1.08±0.075	5.45 (4.78±0.55)	1.8 (1.51±0.17)	0.054 (0.047±0.008)
9	IDSe-4F	1.28	1000	1080	1.51±0.21	1.02±0.076	12.2 (10.7±1.58)	3.8 (3.37±0.50)	0.12 (0.97±0.013)
10	IDSe-4Cl	1.26	1025	1110	1.12±0.18	0.95±0.055	12.4 (10.7±1.25)	3.9 (3.36±0.39)	0.13 (0.10±0.017)
11	Y-2W-F		1035	1140		1.07±0.082	1.53 (1.25±0.16)	0.48 (0.39±0.050)	0.006 (0.005±0.001)
12	SiOTIC-4F	1.24	1050	1120	0.26±0.12	0.91±0.049	2.89 (2.19±0.50)	0.91 (0.69±0.16)	0.031 (0.026±0.007)
13	Y-2W-Th		1055	~		1.08±0.075	0.26 (0.24±0.04)	0.08 (0.075±0.012)	0.006 (0.005±0.001)
14	COTIC-4F	1.17	1125	1200	0.38±0.14	0.78±0.041	2.81 (2.43±0.39)	0.88 (0.75±0.12)	0.031 (0.024±0.006)
15	TTT-C20-4F		1150	~		1.11±0.075	1.84 (1.70±0.16)	0.59 (0.54±0.050)	0.017 (0.016±0.002)

a) Average values with standard deviation were obtained from four measurements.

b) Values shown in brackets are averages over 15 devices for each emitter.

Supplementary Files

This is a list of supplementary files associated with this preprint. Click to download.

- SupplementaryInformation.docx
- Sup.Video3.mp4
- Sup.Video2.mp4
- Sup.Video1.mp4